Energy 112 (2016) 52–66

Contents lists available at ScienceDirect

Energy

journal homepage: www.elsevier.com/locate/energy

Modeling, control, and dynamic performance analysis of a reverse osmosis desalination plant integrated within hybrid energy systems

Jong Suk Kim*, Jun Chen, Humberto E. Garcia

Idaho National Laboratory, 750 University Boulevard, Idaho Falls, ID 83415-3570, USA

ARTICLE INFO

Article history:
Received 25 September 2015
Received in revised form
19 April 2016
Accepted 15 May 2016

Keywords:
Desalination
Reverse osmosis
Variable renewable generation
Hybrid energy systems
Flexible load resource
Ancillary service

ABSTRACT

An RO (reverse osmosis) desalination plant is proposed as an effective, FLR (flexible load resource) to be integrated into HES (hybrid energy systems) to support various types of ancillary services to the electric grid, under variable operating conditions. To study the dynamic analysis of such system, special attention is given here to the detailed dynamic modeling and control design of RO desalination process that employs a spiral-wound membrane module. In particular, the solution-diffusion model modified with the concentration polarization theory is applied to predict RO performance over a large range of operating conditions. Simulation results involving several case studies suggest that an RO desalination plant can provide operational flexibility to participate in energy management at the utility scale by dynamically optimizing the use of excess electrical energy. The incorporation of additional commodity (fresh water) produced from a FLR allows a broader range of HES operations for maximizing overall system performance and profitability.

Published by Elsevier Ltd.

1. Introduction

The U.S. electricity grid is evolving due to changes in society's concerns for global climate change. The major cause of global climate change is generally accepted to be the growing emissions of GHG (greenhouse gas) as a result of fossil fuels use [1]. The global electricity supply sector generates the largest share of GHG emissions (38% of total CO_2 emissions), while the transportation sector contributes 34%, the industrial manufacturing sector 18%, and residential and commercial heating sector 10% [2]. The electric power industry is adding significant capacities of non-emitting, variable REN (renewable) energy sources, especially wind and PV (photovoltaic) solar. Those additions are helping stakeholders meet state Renewable Portfolio Standards [3] and will aid in meeting U.S. federal goals for reduced emissions.

Daily and seasonal load variations are currently managed on the grid through the use of dispatchable generation (i.e., generation technologies that can be turned up, down, on, and off to match the load) [4]. Increasing penetration of variable REN generation raises technical and economic challenges in terms of electric grid integration and stability due to the increasing variability and uncertainty in net load[1] [6–8]. In general, up to approximately 20% penetrations of variable REN generation can be accommodated through the use of operating reserves and other ancillary services[2] [9,10]. Beyond a 20% penetration level, additional flexible generation or other methods are required to manage the variability. Potential solutions include making residential/commercial and industrial loads more responsive, and adding compensatory energy storage to the system.

Typical load-following flexible facilities (e.g., simple-cycle gas turbines) do not operate at full capacities because they operate to meet intermediate or peaking load [3]. On the other hand, electricity-only baseload generators[3] (e.g., nuclear power and fossil fuel-fired combined cycle power plants) often pay the grid to take electricity if they are not able to reduce power when requested by the ISO (independent system operator) due to increased deployment of REN generation and production tax credits[4]; they result in

[1] Net load is the remaining demand that must be met by conventional generation sources after variable generation is subtracted from the total load (demand) [5].

[2] Ancillary services are functions performed by generation (and possibly responsive load) to support the basic services of the electric grid, including balance of generation and load in near real-time.

[3] Baseload generators are high-capital-cost low-operating-cost technologies that should operate at full capacities to maximize profits.

[4] Production tax credits are a federal incentive that provides financial support for the first ten years of a REN energy facility's operation [5].

* Corresponding author. Tel.: +1 208 526 1332; fax: +1 208 526 3150.
E-mail addresses: jkim0916@gmail.com, jongsuk.kim@inl.gov (J.S. Kim).

http://dx.doi.org/10.1016/j.energy.2016.05.050
0360-5442/Published by Elsevier Ltd.

cost and regulatory inefficiencies for many hours during the year. Even though flexible operation of electricity-only baseload generators is technically achievable and is currently conducted in certain regions, this operational mode is not recommended based on cost, profitability, and safety considerations [5]. This requires new technology and energy systems deployment approaches that could utilize excess plant capacity (thermal and/or electrical), when REN generation is active and/or electrical demand is low, for value-added processes beyond electricity production. Consequently, the questions for the future electricity grid are how to utilize available energy resources in an efficient and cost-effective manner with capital-intensive electric generating assets (1) to generate economical "load-following" power in a "load-dynamic" manner (2) to improve grid flexibility and support various types of ancillary services (in wholesale electricity markets), and (3) to produce additional commodities for the combined electricity, industrial manufacturing, and transportation sectors, thus promoting competitive manufacturing approaches [3,9]. One such energy solution is a "hybrid" energy system, which, in this paper, is defined as a single facility that produces multiple products – with at least one being an energy commodity such as electricity, transportation fuels, hydrogen/oxygen gas mixture, and fresh water – from multiple energy inputs using complementary energy conversion subsystems [3,5,11].

The unique aspect of the concept of industrial scale HES (hybrid energy systems) with high REN energy penetration (greater than 20% of HES generation capacity), with respect to electric grid integration and stability, is their ability to provide various types of ancillary services (e.g., regulating, ramping, load following, and contingency reserve) while allowing operation of both REN and baseload generation sources at levels that maximize economic benefit. As energy conversion subsystems are internally coupled and share the same interconnection within the given HES configurations, they are integrated "behind" the electrical transmission bus [5]. This requires industrial scale plants effectively acting as FLRs (flexible load resources) within the given HES configurations to operate under highly flexible conditions, as opposed to their typical (constant) operating conditions. In many cases these FLRs can respond to changing net load more rapidly than generators. The key operating properties in determining the adequacy of FLRs for supporting various ancillary services to the electric grid include [12]:

- Initial response time: The time it takes to respond to a change in a power set-point.
- Ramp rate: The rate at which the amount of power consumption can change.
- Settling time: The time it takes to settle after a power set-point change.
- Duration: The time during which the FLR must be able to maintain the required change in a power set-point after settling time.
- Power capacity: The total rated power for the FLR. The size ranges from kilowatts to megawatts and is important for establishing the amount of response available during any given instant.
- Minimum turndown: The lowest operating point, after which the FLR must turn off. A higher minimum turndown reduces the amount of power capacity that can be used for supporting ancillary services.

Several types of FLRs suitable for HES applications include:

- Steam electrolysis to produce hydrogen/oxygen gas mixture [13],
- Natural gas reforming to produce various commodities: hydrogen, ammonia, methanol, olefins, and synthetic fuels [9,13–16],
- Coal-to-liquid synthetic fuels [15], and
- Desalination to produce portable (fresh) water [11,17–21].

Among the above applications, desalination, in particular via RO (reverse osmosis) process, is perceived as an attractive option for a FLR as its electrical integration with HES exhibits relatively low-order complexity. Furthermore, an RO desalination plant (or simply referred to as an RO plant) can be operated at its minimum turndown for as long as requested [18].

In this work, a HES concept – whose core capability is the ability to utilize an excess generation capacity at times of reduced grid demand and/or of increased REN generation to produce clean fresh water via RO desalination – is considered. The primary objective is to investigate the dynamic performance characteristics of an RO plant integrated within HES configurations under flexible operation. Since the implications of high variability and uncertainty in the time-varying REN energy generation and electricity demand can only be effectively understood in a dynamic setting, it is essential to develop a detailed "dynamic" model of a highly responsive load (i.e., RO plant) in the considered HES. Several tests are carried out to demonstrate its capability to manage the high variability of REN generation and/or electricity demand (load) – while supporting (1) a commodity production (i.e., fresh water) with desired quality level and (2) ancillary services as needed by the electric grid. In particular, the RO system technical performance is evaluated in terms of response time, ramp rate, and load-following response. In the case studies addressed here, the VEL (variable electrical load) requested to an RO plant by a supervisory controller is compared to the actual power consumption in RO process. Furthermore, the RO performance indicators – such as salinity; salt rejection; fresh water flow rate; and controlled feed (operating) pressure associated with a HP (high-pressure) feed pump, which in turn affects the quality and throughput of the fresh water – are monitored accordingly. Note that the mathematical model is developed for applications for both seawater RO and BWRO (brackish water reverse osmosis) desalination. However, the case studies are developed based on options considered in Refs. [11,18], in which a nuclear-solar PV hybrid energy system was proposed as a regional option in Arizona to support the production of fresh water via a BWRO plant[5]; the application of this work is limited to BWRO desalination.

The reminder of this paper is organized as follows. The HES option considered in this study is presented in Section 2. Section 3 presents the dynamic model development and regulatory control strategies for RO desalination process. This section also briefly describes the key assumptions made in sizing the HES and their individual components for the case studies. Section 4 provides the case studies results with detailed discussion involving dynamic performance of RO desalination, under variable REN generation. Finally, Section 5 concludes this paper.

2. HES configuration

HES can have diverse purposes and configurations. In this work, a particular HES option is envisioned to be an industrial microgrid connected to the power grid as illustrated in Fig. 1, which includes several components: a PHG (primary heat generation) plant, a TEC (thermal-to-electrical conversion) system, a REN power generation

[5] The Navajo reservation is located in the northeast corner of Arizona and contains 250 million acre-feet [81.5 trillion gallons] of brackish water.

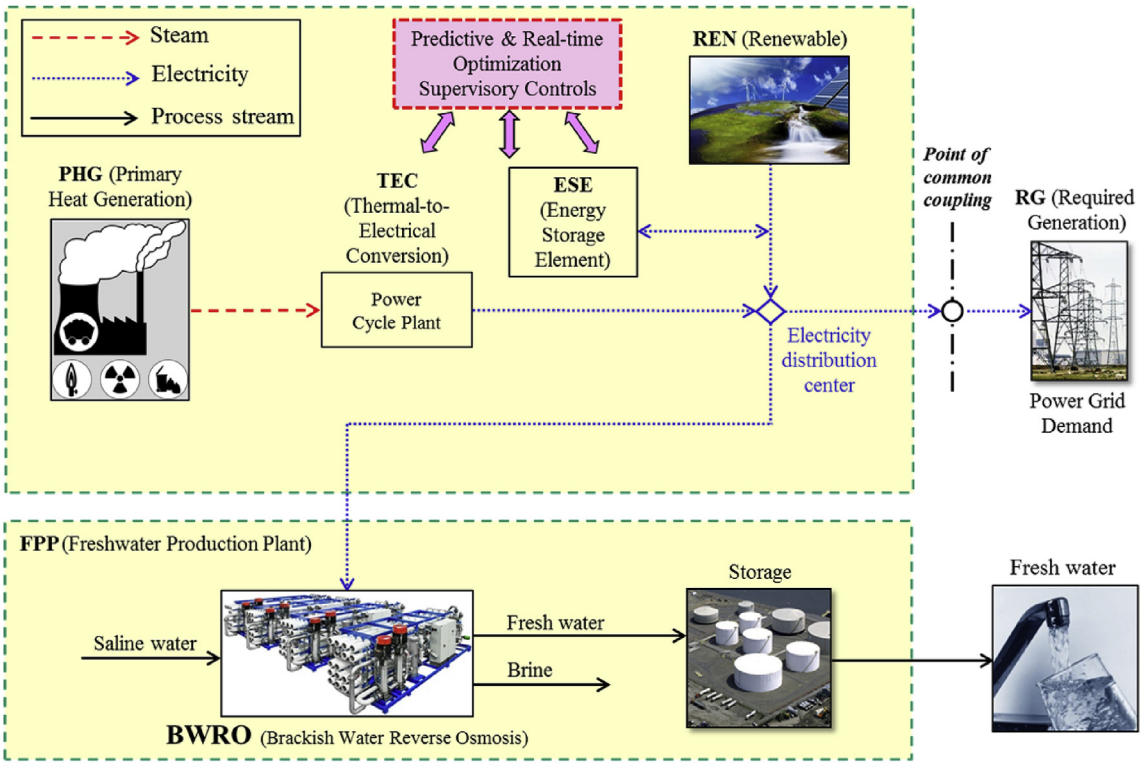

Fig. 1. Architectural topology of the considered HES.

system, an ESE (energy storage element), a FPP (freshwater production plant), and the power grid. PHG is the primary source of energy for the considered HES and can be either nuclear fuel- or fossil fuel-based steam production plant. The steam produced from a PHG plant is delivered to a TEC system, which is the primary source of electricity. A TEC system can be a Brayton or/and Rankine power cycle(s) and produces the RG (required generation) for meeting the grid demand, considering (1) the contribution received from REN sources (e.g., PV solar or wind) and (2) the electricity delivered to a FLR (i.e., a BWRO plant). Notice that RG is subtracted from the total electricity generation, yielding an excess generating capacity that could be utilized to produce other energy currencies in addition to electricity. As opposed to conventional single-output generators that would typically require variation in baseload power generation in the presence of variable renewable generation and/or demand, HES units can maintain baseload generation by diverting excess energy to produce alternative commodities at times of reduced grid demand and/or of increased REN generation. In this work, this excess electrical power is directed to a FPP.

RO desalination utilizes a semi-permeable membrane, which allows water to pass through but not salts, thus separating the fresh water from the saline feed water. A typical BWRO plant (see Fig. 2(a)) consists of four main components: feed water pretreatment, HP pumping, membrane separation, and permeate post-treatment. Fig. 2(b) depicts the configuration of an RO vessel (a multi-element module) used in RO desalination, which typically comprises of six to eight membrane modules connected in series. The concentrate water rejected by the first membrane module plays a role as the feed water for the second membrane module by the successive order, and so on. These pressure vessels are arranged in rows in each membrane stage, with two-stage membrane separation being typical in BWRO. Each stage has a recovery of 50–60%, achieving overall system recovery of 70–85%.

As shown in Fig. 1, the REN power output may be introduced to the electricity distribution center via an ESE (e.g., a flywheel or a electric battery), or directly. Considering the fact that REN generation is usually characterized by high variability, intermittency, and non-dispatchability, an ESE could be included within HES in order to perform power smoothing. Note that the levelized cost of REN generation would be reduced when a FPP replaces an ESE completely. However, excluding an ESE from HES can result increased operations and maintenance costs and potentially shortened FPP life because the equipment (e.g., control valves, pumps, and RO membrane modules) would wear out at much faster rates in responding directly to highly variable REN sources. The potential impact of integration of an ESE within HES on the operational lifetime of a FPP requires additional study, which is beyond the scope of this paper.

The considered HES configuration is connected to the electric grid via a point of common coupling. Under supervisory control, the two electricity generation units, i.e., (1) PHG-TEC (PHG coupled with TEC) and (2) REN power generation coupled with an ESE, are operated accordingly to deliver the electricity generation requested by the electric grid operator, e.g., an ISO or a regional transmission organization. Alternatively, the system supervisor can determine the time-varying electrical demand profiles in response to price variations in electricity, alternative product(s), and feedstock(s), thus supporting economic optimization for operations, e.g., NPV (net present value). In either case, the power delivered to the electric grid is limited by a maximum rated generation capacity of a PHG-TEC system and the minimum turndown of a FPP.

3. Model description and development

This section introduces the detailed dynamic modeling and regulatory (low-level) control strategies of an RO plant. Also, the key assumptions made in sizing the HES and its individual components for the case studies (discussed in Section 4) are provided.

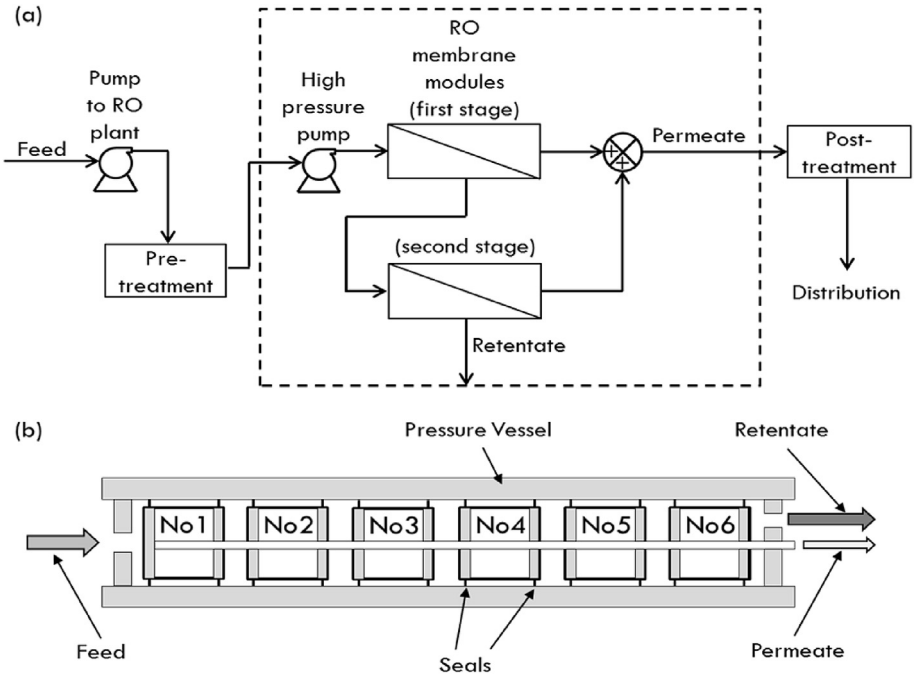

Fig. 2. RO desalination: (a) process flow diagram for a two-stage BWRO plant and (b) schematic of an RO vessel, which consists of six membrane modules in series [18].

3.1. RO plant

The modeling efforts of RO desalination process are focused on the two main components, i.e., HP pumping and membrane separation, enclosed in the dashed box shown in Fig. 2(a).

3.1.1. Dynamic modeling of a spiral-wound module

Commercially available RO membrane modules include spiral-wound, hollow-fiber, tubular, plate-and-frame, and monolithic modules, amongst which a spiral-wound module[6] is the most popular in industry due to its high membrane area to volume ratio (specific surface area), ease of operation, and high permeation rate [22]. Spiral-wound modules are made from flat membrane envelopes, wrapped around a central collection tube as seen in Fig. 3. Saline water passes along the length of the module and permeate water spirals inwardly through the permeate envelope to the central collection tube. As only a portion of the feed passes through the membrane, the feed becomes increasingly concentrated from the beginning to the end of the brine channel, resulting in an increase in osmotic pressure along the channel. Both the feed and the permeate are transported through the module in fluid-conductive spacer material [23]. Spacers are placed in the retentate and permeate channels in order to reduce the void volumes of both channels and enhance the effective velocities [24]. Modern modules typically contain a multiple number of membrane sheets (also referred to as “leaves” or “elements”), yielding a large specific area.

A dynamic RO model is developed based on the work shown in Ref. [25], which describes the steady-state behavior of SWRO (spiral-wound reverse osmosis) process, to describe the process dynamics over a wide range of operating conditions. The main assumptions made for the model derivation are as follows:

- The solution-diffusion model (one of the most commonly used models in RO system design [26]) is valid for the transport of solute (salt) and solvent (water) through the membrane.
- An RO membrane module is non-porous and is made up of flat channels with spacers.
- The thin film theory is valid for calculating concentration polarization effect.
- The brine only flows along the z-axis (axial), i.e., the flow perpendicular to the bulk flow along the p-axis (spiral) is neglected. The permeate velocity along the z-axis is negligible.
- The glued area of the membrane (see Fig. 3) is ignored, i.e., $w_{BR} = w_m$ and $l_{BR} = l_m$.
- Feed-spacer thickness is approximated by the height of the brine channel, i.e., $h_{sp} = h_{BR}$.
- Immediate and complete mixing of the locally produced permeate water with the bulk flow in the permeate channel is assumed.
- Pressure drop in permeate side is neglected.
- Hydraulic pressure drop due to wall friction, solute concentration, and fluid temperature and velocity at brine side vary linearly in axial direction. Consequently, space-dependent effects on those operating variables are averaged by arithmetic mean.
- Of the various possible dissolved components in feed stream, the only components considered are Na^+ and Cl^-; therefore, the mass concentration of TDS (total dissolved solids) in the feed stream is the same as that of NaCl.
- The effect of feed pH on the RO system performance is ignored.
- Driesner's correlations [27] are used to calculate the thermodynamic properties for saline fluids in the binary H_2O–NaCl system.
- Empirical equations, which are provided in Appendix A, are used to estimate the saline water properties, i.e., D_{NaCl} and μ_{NaCl} [28,29].

For a SWRO module, dynamic equations for the solute density, solute concentration, and specific internal energy are defined as follows based on the laws of mass and energy conservation:

[6] A disadvantage of spiral-wound modules is that rapid fouling of the spacer channels with particulate matter can occur.

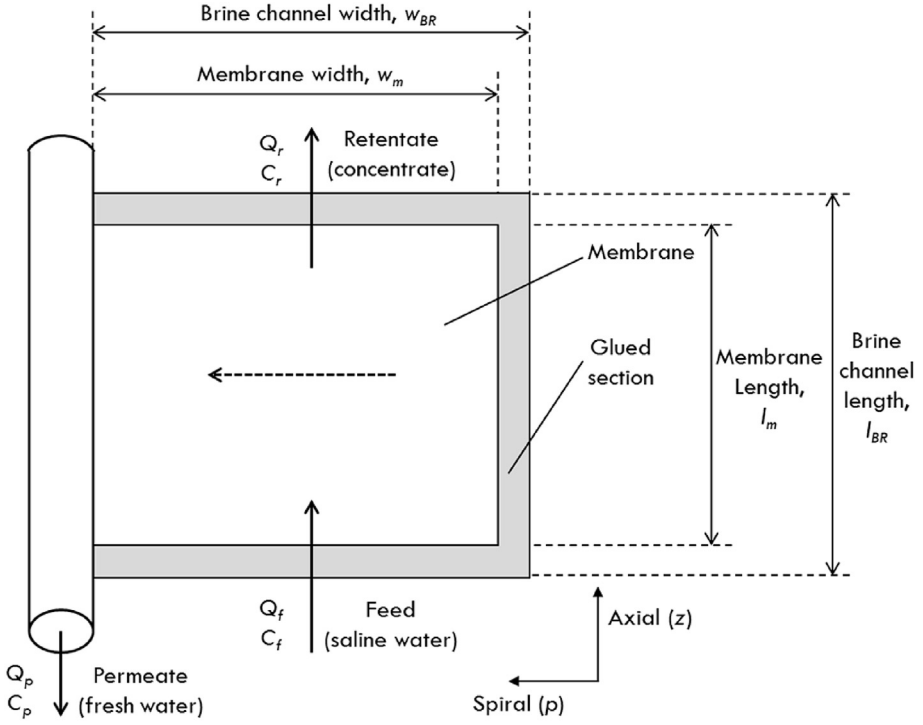

Fig. 3. A schematic diagram for a spiral-wound module.

$$V_{BR}\frac{d\rho_{b,t}}{dt} = Q_{f,t}\rho_{f,t} - Q_{r,t}\rho_{r,t} - Q_{p,t}\rho_{p,t} \tag{1}$$

$$V_{BR}\frac{dC_{b,t}}{dt} = Q_{f,t}C_{f,t} - Q_{r,t}C_{r,t} - Q_{p,t}C_{p,t} \tag{2}$$

$$V_{BR}\frac{d\left(\rho_{b,t}\widehat{u}_{b,t}\right)}{dt} = Q_{f,t}\rho_{f,t}\widehat{h}_{f,t} - Q_{r,t}\rho_{r,t}\widehat{h}_{r,t} - Q_{p,t}\rho_{p,t}\widehat{h}_{p,t} \tag{3}$$

where

$$V_{BR} = n_l w_{BR} h_{BR} l_{BR} \phi_{BR} \tag{4}$$

Eqs. (5) and (6) relate the axial velocities to the volumetric flow rates at brine side as follows:

$$v_{zf,t} = \frac{Q_{f,t}}{n_l w_{BR} h_{BR} \phi_{BR}} \quad \text{at } z = 0 \tag{5}$$

$$v_{zr,t} = \frac{Q_{r,t}}{n_l w_{BR} h_{BR} \phi_{BR}} \quad \text{at } z = l_{BR} \tag{6}$$

The volumetric flow rate of the permeate water (Q_p) depends on the local solvent flux (J_{vz}):

$$Q_p = 2n_l w_{BR} \int_0^{l_{BR}} J_{vz} dz \tag{7}$$

According to the classical solution-diffusion model, the average solvent flux (Eq. (8)) and solute flux of species i (Eq. (9)) through the membrane are given as follows [25,30]:

$$\bar{J}_v = L_v\left(\Delta p - \sum_i \Delta\pi_i\right) \text{ at } z = l_{BR}/2, \quad \forall i \in \left\{Na^+, Cl^-\right\} \tag{8}$$

$$\bar{J}_{s,i} = \bar{J}_v\frac{C_{p,i}}{MW_i} = L_{s,i}\left(\frac{\overline{C}_{m,i} - C_{p,i}}{MW_i}\right) \text{ at } z = l_{BR}/2, \quad \forall i \in \left\{Na^+, Cl^-\right\} \tag{9}$$

subject to

$$L_v = L_{v0}\exp\left[\frac{\alpha_1(T_b - 293)}{293} - \alpha_2 p_f\right]\left(1 - \frac{A_s}{A_m}\right) \tag{10}$$

$$L_{s,i} = L_{s0,i}\exp\left[\frac{\beta_1(T_b - 293)}{293}\right], \quad \forall i \in \left\{Na^+, Cl^-\right\} \tag{11}$$

$$\Delta p = p_f - p_p - \frac{\Delta p_{hydr}}{2} \text{ at } z = l_{BR}/2 \tag{12}$$

$$\Delta\pi_i = \left(\frac{\overline{C}_{m,i} - C_{p,i}}{MW_i}\right)RT, \quad \forall i \in \left\{Na^+, Cl^-\right\} \tag{13}$$

$$\overline{C}_{m,i} = \frac{C_{m,i}|_{z=0} + C_{m,i}|_{z=l_{BR}}}{2}, \quad \forall i \in \left\{Na^+, Cl^-\right\} \tag{14}$$

$$T_b = \frac{T_f + T_r}{2} \tag{15}$$

Eq. (8) implies that water permeation across the membrane depends on applied hydraulic pressure difference (Δp) and the sum of the osmotic pressures difference of dissolved solids in an aqueous solution of NaCl ($\sum\Delta\pi_i$). The calculation of the Δp_{hydr} (hydraulic pressure loss along a spiral-wound element due to wall

friction), shown in Eq. (12), is summarized in Appendix B [31]. Eq. (9) states that the solute transport by diffusion is proportional to a concentration gradient only, and thus is independent of the Δp across the membrane [32,33]. Accordingly, the higher the Δp, the purer the permeate water. Similarly, the osmotic pressure (Eq. (13)) is proportional to the solute concentration [33–35]. The relationship between the average solute flux and the average solvent flux is also defined in Eq. (9).

During reverse osmosis, a concentration build-up of the retained material occurs in the boundary layer close to the membrane, resulting in the difference between the solute concentration at the membrane surface and that in the bulk phase. This phenomenon is referred as the "concentration polarization," which results in a higher osmotic pressure difference across the membrane. On the basis of the thin-film theory and from Fick's law for diffusion, the concentration at the membrane surface can be derived as follows [36–39]:

$$\frac{C_m - C_p}{C_b - C_p} = \exp\left(\frac{J_v}{k_{NaCl}}\right) \tag{16}$$

where k_{NaCl} is the mass transfer coefficient for the back diffusion of NaCl from the membrane to the bulk solution at brine side and can be estimated by an empirical Sherwood relationship [31]:

$$k_{NaCl} = 0.065\left(\frac{\rho_b v_{zb} d_h}{\mu_{NaCl}}\right)^{0.875}\left(\frac{\mu_{NaCl}}{\rho_b D_{NaCl}}\right)^{0.25}\left(\frac{D_{NaCl}}{d_h}\right) \tag{17}$$

For flow channels with non-circular geometry, the hydraulic diameter of spacer-filled flow channels (d_h) is defined as follows [24,31]:

$$d_h = \frac{4\phi_{BR}}{\frac{2}{h_{sp}} + (1-\phi_{BR})a_{sp}} \tag{18}$$

$$a_{sp} = \frac{8}{h_{sp}} \tag{19}$$

The two important parameters reflecting the performance of an RO membrane or an overall RO system are the water recovery R_w and the salt rejection R_s:

$$R_w(\%) = \frac{Q_p}{Q_f} \times 100 \tag{20}$$

$$R_s(\%) = \left(1 - \frac{C_p}{C_b}\right) \times 100 \tag{21}$$

R_w quantifies the fraction of influent water recovered in the permeate. R_s is a characteristic often used by RO membrane manufactures to describe membrane rejection properties. Typically, RO membranes achieve NaCl rejections of 98–99.8% [40].

Although Eqs. (1)–(21) have been used to determine the permeate flow rate and quality for each membrane module, they can be used to predict the same behavior for pressurized RO vessels, which contain more than one membrane modules in series as follows:

$$X_{r,j} = X_{f,j+1}, \quad j = 1,2,\ldots, N_M - 1, \quad \forall X \in \left\{Q,\ C,\ \widehat{h},\ p\right\} \tag{22}$$

$$p_{r,j} = p_{f,j} - \Delta p_{hydr,j}, \quad j = 1,2,\ldots,N_M \tag{23}$$

$$\rho_p Q_p = \sum_{k=1}^{N_{ST}} \rho_{p,k} Q_{p,k} \tag{24}$$

$$C_p = \frac{\sum_{k=1}^{N_{ST}} C_{p,k} Q_{p,k}}{Q_p} \tag{25}$$

For given feed conditions and the membrane-specific model parameters (e.g., intrinsic solvent and solute transport parameters), the resulting operating variables (e.g., pressures, flow rates, and concentrations at permeate and brine sides) and the key RO performance parameters (e.g., water recovery and salt rejection) can be calculated by Eqs. (1)–(25) subject to a number of system operating constraints as follows:

$$S_{p,t} \le S_p^{max} \tag{26}$$

$$v_f^{min} \le v_{f,j,t} \le v_f^{max}, \quad j = 1,2,\ldots,N_M \tag{27}$$

$$p_f^{min} \le p_{f,j,t} \le p_f^{max}, \quad j = 1,2,\ldots,N_M \tag{28}$$

$$T_f^{min} \le T_{f,j,t} \le T_f^{max}, \quad j = 1,2,\ldots,N_M \tag{29}$$

$$\sum_i \Delta\pi_{i,j,t}^{exit} \le \Delta p_{j,t}^{exit}, \quad j = 1,2,\ldots,N_M, \quad \forall i \in \left\{Na^+, Cl^-\right\} \tag{30}$$

Eq. (26) enforces the maximum salinity of the permeate so as to satisfy the drinking water standard for TDS at any given time. Eqs. (27)–(29) represent the RO system operating constraints such as minimum/maximum feed velocity, pressure, and temperature. Eq. (30) is the so-called "thermodynamic restriction[7]" of cross-flow membrane RO desalting [41,42]. This inequality implies that in order to ensure permeate productivity, along the entire membrane module, the applied hydraulic pressure difference should not be less than the sum of the osmotic pressures difference at the module exit.

In this work, brackish water RO desalination is considered to support the production of fresh water via the FilmTech 8" BW30-400 membrane, which is a spiral-wound module manufactured by Dow Chemical. The specifications of this particular membrane chosen for simulation can be found in Table C.1 in Appendix C. In all case studies, pretreated feed water at 298.15 K and 1 atm, and with a constant salinity value of 3500 ppm of TDS is assumed to be available; therefore, the only energy use of RO process is the energy consumption by the HP pumps. At these feed conditions, the BWRO plant is sized for 15.66 $m^3\ s^{-1}$ (357.4 MGPD [million gallons per day]) capacity, about four times the size of one of the current largest seawater RO desalination systems [43]. A plant with this capacity consumes 45 MW_e of electrical power to generate the required feed (operating) pressure (16.5 barg) for desalting the brackish water, containing 3500 ppm of TDS. Table 1 reports design specifications of the BWRO plant considered in this work.

3.1.2. Regulatory control

As illustrated in Fig. 1, HES exploit a hierarchical control strategy. This high-level control strategy dynamically determines electricity

[7] The osmotic pressure of the concentrate significantly increases downstream in the RO channel such that when the osmotic pressure difference equals to the applied pressure difference, water production beyond that portion of the RO channel vanishes. This phenomenon is referred to as the "thermodynamic restriction" in the current work.

Table 1
BWRO plant specifications.

Symbol	Description	Unit	Value
N_{pump}	Number of HP feed pumps, each of which is rated at 1 MW_e	–	45
ε_{pump}	Pump efficiency	%	80
ω	Pump shaft rotational speed	rpm	2240
V_{op}	Valve opening	%	80
N_{TR}	Number of RO unit trains	–	45
N_{VE}	Number of pressure vessels per one RO unit train	–	220
N_{ST}	Number of stages	–	2
N_M	Number of RO modules per one pressure vessel (or stage)	–	6
T_f	Feed temperature	K	298.15[a]
S_f	Feed salinity	ppm	3500[a]
p_f	Feed (operating) pressure	barg	16.5
p_p	Permeate pressure	barg	0[a]
Q_p	Permeate volumetric flow rate	$m^3\ s^{-1}$ [MGPD]	15.66 [357.4]
$P_{l,\ RO,\ n}$	Rated electrical load in the FPP	MW_e	45
$\overline{S}_p$	Average permeate salinity (quality)	ppm	60
R_S	Salt rejection	%	99.2
R_{w1}	Water recovery in the first stage	%	48
R_{w2}	Water recovery in the second stage	%	46
R_w	Overall water recovery	%	72

[a] They are assumed to be constant for the sake of simplicity, although the model can account for variable feed conditions.

delivered to the FPP and updates set points of the local controllers accordingly, in order to ensure the electricity distributions into the electric grid versus the FPP meet the supply requirements.

Fig. 4 depicts the network for a large-scale BWRO desalination system. The RO network consists of multiple parallel RO unit trains (physically packed groups of RO vessels arranged in row), each of which contains a HP feed pump supplying the pretreated feed water to hundreds of RO vessels. Each RO unit train is assumed to operate under the same operational conditions (i.e., temperature, pressure, flow rate, and concentration) for the sake of modeling simplicity, although they are not exactly the same. The same assumption is valid for the RO vessels arranged in parallel rows in an individual RO unit train. With these assumptions, regulatory control strategies (single-input single-output control scheme) for a BWRO desalination system are developed (see Fig. 5) to achieve two control objectives: (1) meet the power consumption requested by the system supervisor $L_{E,\ sp}$, i.e., VEL, and (2) to maintain feed (operating) pressure at the desired value (or set point) $p_{f,\ sp}$. While the former is met by adjusting the pump shaft rotational speed ω, the latter can be controlled by adjusting the opening of the pneumatic PCV (pressure control valve) V_{op} located in the retentate stream. This control scheme ensures that the permeate quality (or salt rejection) is maintained within the desired limits, regardless of the change in the VEL requested to the desalination plant by a supervisory controller.

Among the various techniques available to determine controller

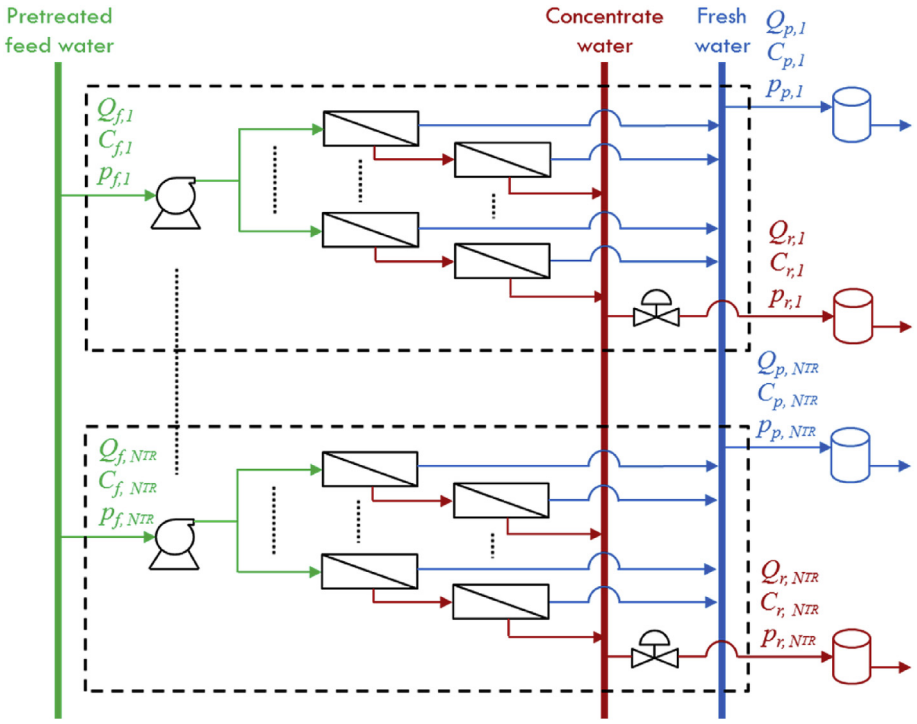

Fig. 4. RO network for brackish water desalination, where each dashed box represents one RO unit train. N_{TR} is the number of RO unit trains in the RO network.

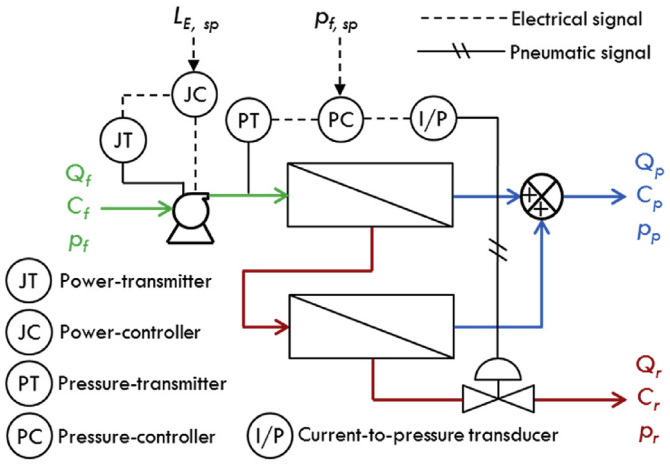

Fig. 5. A control schematic of an RO unit train, with two-stage membrane separation.

feedback settings, such as DS (direct synthesis) method, internal model control method, controller tuning relations, and frequency response techniques, the DS method is employed to tune the PI (proportional-integral) controller settings with the assumptions that the process models are approximated by the FOPTD (first-order-plus-time-delay) model and are perfect. The results are summarized in Table C.2 in Appendix C. For detailed reading on the DS method, see Ref. [44].

3.2. PHG, TEC, and RG

The PHG plant operates at full thermal generation rate, generating an equivalent electrical power of 180 MW_e via the TEC system. Under the extreme situation that the electric grid requests from a hybrid energy system a RG of 165 MW_e (the maximum electric load on the demand side that the system can satisfy) in the absence of REN penetration, the electrical power directed to a freshwater desalination plant is 15 MW_e. In other words, the minimum turndown of an RO plant is 15 MW_e, ensuring that the RO plant is operated continuously with a minimum load, even when no REN power is provided to the system.

3.3. REN energy

For REN energy systems, the two separate systems are considered: (1) a PV system, which converts solar energy into direct current electricity using semiconducting materials and (2) a wind farm, which convert the kinetic energy in the wind into mechanical power or electricity via a generator. REN energy generation is modeled as a time-series input signal to an ESE based on solar irradiance and ambient temperature data for a PV system or based on wind speed data for a wind farm. Historical data of solar irradiance and ambient temperature at Southwest Solar Research Park in Phoenix,[8] Arizona and that of wind speed measured in West Texas[9] were obtained from National Renewable Energy Laboratory database and used in the case studies. For the mathematical models and the values of model parameters used to calculate PV solar and wind powers in this work, see Refs. [45–51].

For the case studies, each individual PV module is sized such that it can provide maximum of 4 MW_e rated power at the standard test condition. In addition, seven PV modules are assumed to yield the total nominal capacity of 28 MW_e, provided that a linear scaling in REN power with the number of PV modules is valid. Similarly, eight identical wind turbines, each rated at 3.6 MW_e, provide maximum of 28.8 MW_e rated power at full production.

3.4. ESE

The ESE considered in this study is a power-smoothing battery, which removes or smooths the high variability introduced by either PV or wind energy. As an illustration, Fig. 6 shows the original PV electricity generation profile and the filtered PV electricity generation profile with the operation of the electrical battery. It should be noted that with the historical weather data and battery size considered as the bases of this study, at the highest solar irradiance, the maximum amount of PV solar power that can be delivered to a FPP is around 30 MW_e, which is higher than the nominal capacity (28 MW_e). With baseload power generation, the total electric power input to a FPP swings from 15 to 45 MW_e for a PV integrated HES and from 15 to 43.8 MW_e for a wind integrated HES.

4. Dynamic performance of RO desalination

Four case studies (Cases 1–4) were conducted to analyze the dynamic performance of the RO plant integrated within the considered HES. In these case studies, the key process variables ($P_{l,\,RO}$, $L_{E,\,sp}$, p_f, Q_p, S_p, and R_s) are observed to assess whether the dynamic behavior of the RO plant is satisfactory under each test. In all case studies, the proposed HES are modeled dynamically with the object-oriented Modelica language using the Dymola tool and *Modelica. ThermoPower* library [52]. Table 2 lists the simulation setup values used in each case scenario considered in this work.

4.1. Case 1: response time and ramp rate to a 25% step increase in the $L_{E,\,sp}$

In order to assess the response time and ramp rate characteristics of the proposed RO plant, a step change was made in the electrical demand profile in the absence of REN penetration. The transient was initiated at 50 s via a 9 MW_e decrease in electrical grid demand from an initial generation level of 144 MW_e. As the PHG-TEC system generated a constant electrical power of 180 MW_e, this change resulted in an immediate increase of 9 MW_e in the $L_{E,\,sp}$ (from an initial load level of 36 MW_e). Fig. 7 shows the CVs (controlled variables) and MVs (manipulated variables) responses following the step change, exhibiting very short response times and ramp rates in achieving the two control objectives. As seen in Fig. 7(a), it required about 30 s for the consumed power to match

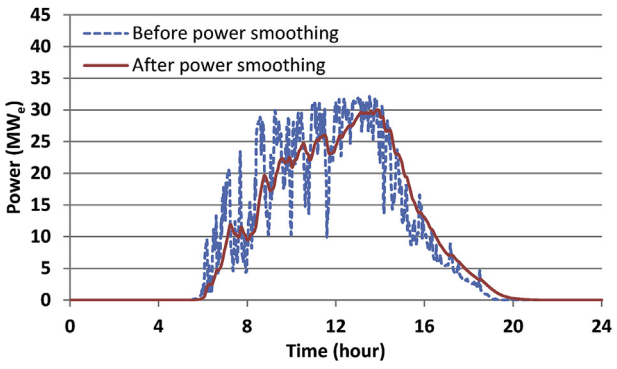

Fig. 6. PV electricity generation profile before and after power smoothing.

[8] Accessed on January 5, 2015 at http://www.nrel.gov/midc/ssrp/.
[9] Accessed on January 7, 2015 at http://www.nrel.gov/electricity/transmission/eastern_wind_dataset.html.

Table 2
Simulation setup values used in the case studies.

Case no.	Electrical generation to grid (MW_e)	Renewable energy		VEL requested to the BWRO, $L_{E,sp}$ (MW_e)	Simulation output interval, Δt (s)
		Type	Generation (MW_e)		
1	144 to135 (step change)	N/A	0	36 to 45 (step change)	0.1
2	165 (constant)	PV solar	0–30	15–45 (variable)	60
3	165 (constant)	Wind	0–28.8	15–43.8 (variable)	60
4	135–165[a] (variable)	PV solar	0–30	15–45[a] (variable)	60

[a] Variable quantities that are optimized for the NPV maximization.

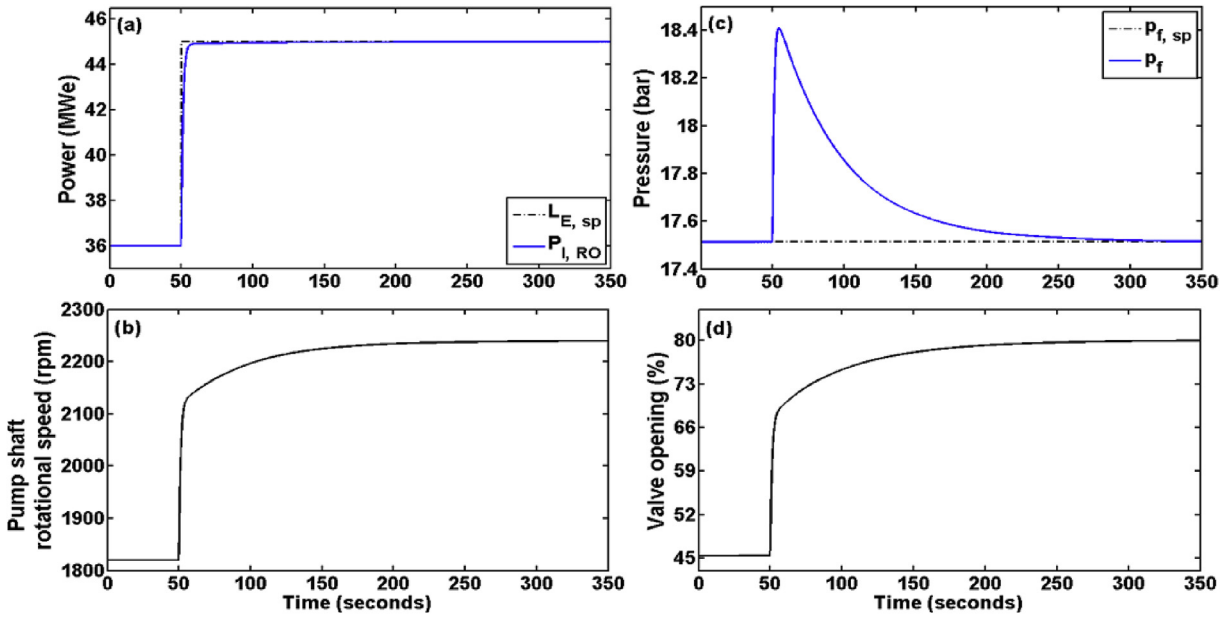

Fig. 7. CVs and MVs responses for Case 1: (a) VEL ($L_{E, sp}$) vs. consumed pump power ($P_{I, RO}$), (b) pump shaft rotational speed (ω), (c) feed pressure set point ($p_{f, sp}$) vs. measured feed pressure (p_f), and (d) valve opening (V_{op}).

the corresponding set-point change and to settle to its final value by adjusting the ω (Fig. 7(b)) accordingly. The PCV quickly increased its opening (Fig. 7(c)) in order to maintain the feed pressure at its constant set-point value of 17.51 bar (Fig. 7(d)) in response to a step change made in the $L_{E, sp}$. The fast response times and ramp rates observed in this case are likely due to the effective control strategies implemented; however, they may also be attributed to the potential absence of engineered operating constraints (imposed for safety, for example) in the model that more realistically characterize all key components of concern. For instance, "water hammer" is produced by a rapid change of flow velocity in the pipelines that may be caused by rapid ramp up/down of pumps and changes in demand condition, sudden valve opening/closure, mechanical failure of a device, etc. Consequently, it could result in violent change of the pressure head, which is then propagated in the pipeline in the form of a fast pressure wave leading to severe damages (such as leakage) [53]. In real application cases, the rates of changes of MVs should be regulated to be slower than those observed in Fig. 8(b) and (d) to prevent water hammer in the pipes; accordingly, the results shown in Fig. 8(a) and (c) would exhibit more sluggish (slower) responses (thus slower settling times) and, possibly, oscillatory behavior. Additional engineering constraints will be incorporated in future model refinement. Nevertheless, these preliminary results strongly suggest that an RO plant, when integrated within HES configurations, can begin responding rapidly and change its response fast enough to participate in the electric grid ancillary services considered, while achieving the control objectives defined in Section 3.1.2.

Fig. 8 shows the corresponding time series for the RO performance indicators: permeate flow rate and salinity, and salt rejection, each of which with respect to the 1st RO vessel (or stage), 2nd RO vessel, and the combination of the two vessels (overall or average). It can be seen from Fig. 8(a) that as the $L_{E, sp}$ increased, so did permeate production rates. This is because as the energy requirement increases at a fixed feed pressure, the feed flow rate increases, resulting in higher solvent flux (permeate flow rate). In Fig. 8(b), the results also show that the solute concentration in permeate (permeate salinity) is inversely proportional to the permeate flux (flow rate). This phenomenon is attributed to the fact that an increased flow rate (thus an increase in the axial velocity) of the bulk solution enhances the back-diffusion of the solute from the membrane surface to the bulk solution on high pressure side of membrane (see Eqs. (16) and (17)). However, increased permeate flux also results in higher transport of solute to the membrane and greater concentration polarization. Under the operating conditions considered in this work, the effect of "back-diffusion" dominates over the effect of "permeate flux" on concentration polarization. Overall, this results in lesser concentration polarization with the higher feed flow rate, and therefore lower permeate salinity and osmotic pressure difference across the membrane. The salt rejections shown in Fig. 8(c) exhibit, as defined by Eq. (21), inversely proportional behavior to the permeate qualities. In other words, the

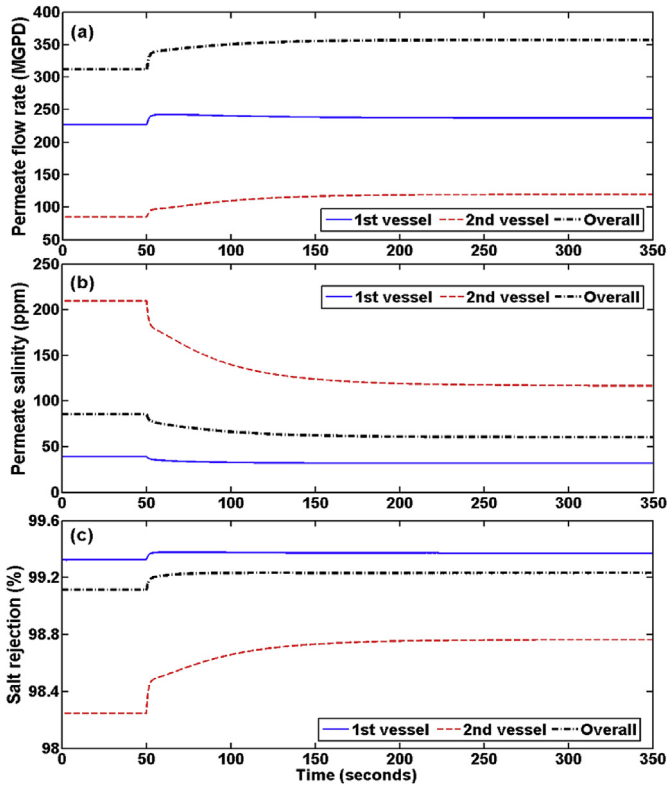

Fig. 8. RO performance indicators for Case 1: (a) permeate flow rate (Q_p), (b) permeate salinity (S_p), and (c) salt rejection (R_s).

higher the feed flow rate, the purer the permeate, provided that the feed pressure remains the same.

Fig. 8 also illustrates the spatial dependency of the permeate flow rate and quality in two-stage RO membrane separation. As feed water passes through an RO membrane element, permeate passes through the membranes, and the remaining water (retentate) becomes more and more concentrated. As the feed/concentrate TDS increase, the salt rejection through the membrane decreases, thus increasing permeate salinity. Therefore, the permeate produced from the 1st vessel (feed entry) has a lower salinity (or higher salt rejection) than the permeate produced from the 2nd vessel (retentate exit). Consequently, in comparison to the 1st RO vessel, the increased permeate salinity resulted in a higher osmotic pressure difference across the 2nd RO vessel, which reduced the permeate flow from the 2nd RO vessel. Such a reduction in permeate flow is also strongly attributed to that a portion of feed water is recovered in the permeate in each RO vessel, yielding a gradually decreasing feed flow available along the RO vessels connected in series.

4.2. Case 2: load-following response with PV solar power

In Case 2, the load-following capability of an RO plant as a FLR under variable PV solar power generation is demonstrated. A constant electricity profile of 165 MW_e delivered from the HES configuration to the electric grid is assumed; thus, a minimum load of 15 MW_e is always distributed to the BWRO plant. Fig. 9 shows the time series of CVs, and the permeate flow rate and quality simulated for one week. As seen in Fig. 9(a), the RO plant can effectively absorb local and instantaneous variability in the REN power source by changing the $L_{E,\,sp}$ accordingly. Notice from Fig. 9(c) and (d) that while the production (Q_p) and concentration (S_p) of fresh water varied as the demand ($L_{E,\,sp}$) varies, the salinity of the fresh water produced was less than a drinking water taste threshold set by U.S. Environmental Protection Agency [43] (i.e., TDS of 500 ppm), ensuring acceptable salt rejection rates over the entire range of RO operating conditions. This is achieved by adequately maintaining the p_f near its desired set point regardless of the VEL diverted to the RO plant (see Fig. 9(b)). These results suggest that the HES, with a high penetration of PV generation, can act as a highly responsive device to meet load-following needs by accordingly delivering the necessary electricity generation profile demanded by the electric grid, while correspondingly adjusting itself to maintain adequate operating conditions. Moreover, since an RO plant can be operated at its minimum turndown for as long as requested, a HES configuration can maintain the change in its electrical production for a long enough duration.

4.3. Case 3: load-following response with wind power

This test is designed to assess the capability of the same system considered in Case 2 for load following, but under wind power generation. The results simulated for one week are plotted in Fig. 10. Similar to the results shown in Case 2, the variability introduced by the REN (wind) source was essentially accommodated by the use of the flexible electrical load provided by the RO plant. As it can be seen, the RO system can closely track the time-varying electrical load (Fig. 10(a)) requested by the system supervisor for freshwater production (Fig. 10(c)), while maintaining the desired feed pressure (Fig. 10(b)) and permeate quality (Fig. 10(d)) at all times.

4.4. Case 4: operational flexibility for economic optimization with PV solar power

In Case 4, the HES configuration, which includes the BWRO plant and PV solar stations, is operated under flexible operational control to optimize the NPV. This scenario used economic optimization function to determine the most advantageous mix of products, resulting in variable electricity generation as a function of the time-dependent wholesale electricity (day-ahead), commodity (fresh water), and feedstock (saline water) prices. The same REN (PV power) generation profile considered in Case 2 (Fig. 11(a)) was assumed in this case, with a constant electrical power generation (net load) of 180 MW_e from the PHG-TEC system (Fig. 11(c)). The models derived for implementing the NPV optimization, and the corresponding cost parameter values assumed in Case 4 can be found from Ref. [54]; therefore, they are not repeated here. The resulting optimal dispatch schedule for a selected one-week period is shown in Fig. 11(b). While operating under the NPV-driven mode, instead of selling surplus power to the grid during the on-peak hours, the operations optimizer maximized the freshwater production (at constant throughput of 357.4 MGPD) with maximum electrical load of 45 MW_e (Fig. 11(d)). This is attributed to the higher net income obtained from freshwater sales than what could have been obtained by participating in wholesale electricity markets, during the considered time period. Based on the cost parameter values reported in Refs. [11,54], where a 600 MW_{th} (thermal) nuclear small modular reactor coupled with Rankine power cycle was selected for a PHG-TEC system, such a system results in the cumulative NPV of about $ 600 million at a real discount rate of 5% for 30 years of operation. The expected payback time for this system is about 15.4 years.

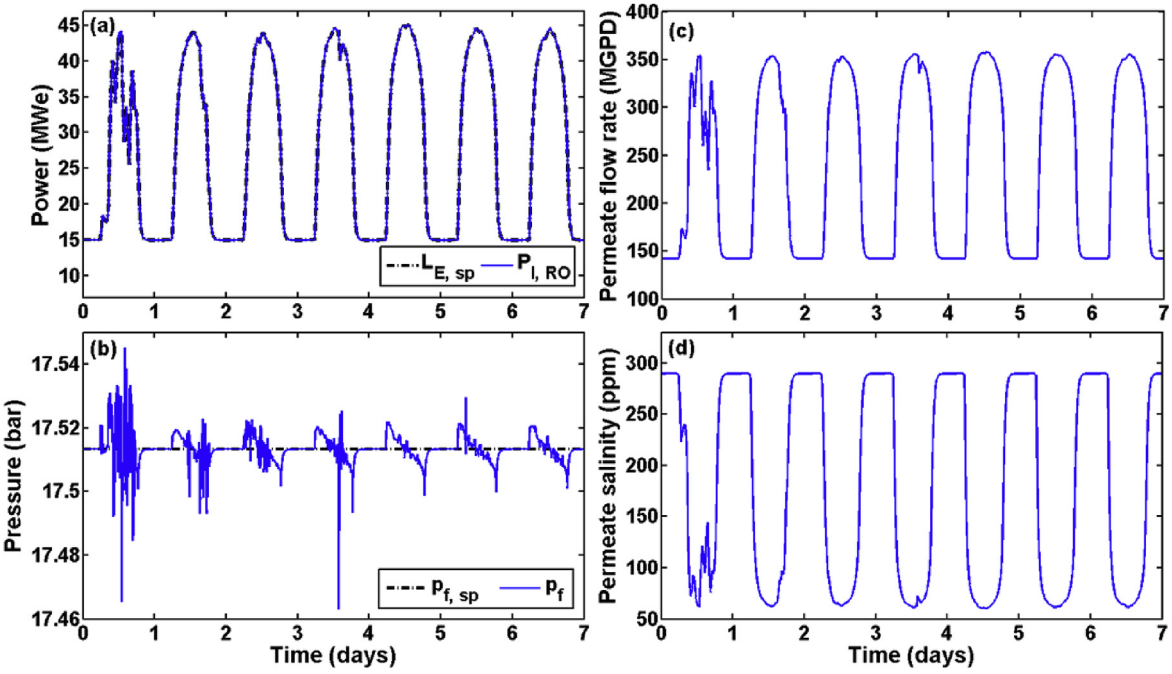

Fig. 9. Output responses to the VEL for Case 2: (a) $L_{E, sp}$ vs. $P_{I, RO}$, (b) $p_{f, sp}$ vs. p_f, (c) Q_p, and (d) S_p.

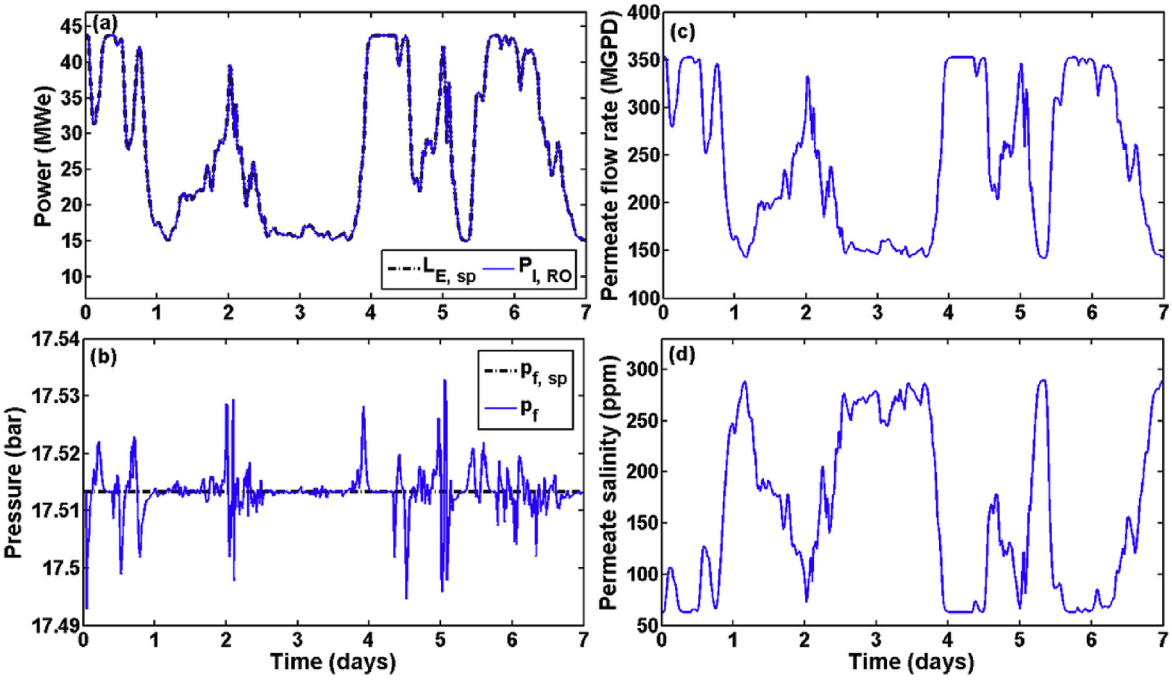

Fig. 10. Output responses to the VEL for Case 3: (a) $L_{E, sp}$ vs. $P_{I, RO}$, (b) $p_{f, sp}$ vs. p_f, (c) Q_p, and (d) S_p.

5. Conclusions

A dynamic performance analysis of an RO desalination plant integrated within HES was carried out to quantify key dynamic characteristics and learn various technical opportunities that may arise from incorporating flexible energy configurations into the electric grid. To support such a dynamic analysis, a detailed dynamic model for RO desalination process, which employs a spiral-wound membrane module, and the corresponding control design have been developed. The case studies results show that an RO plant, when integrated within HES, can respond quickly, settle sufficiently fast, and maintain the required change for a long enough duration in response to large, fast change in the VEL, in support of various types of ancillary services such as operating

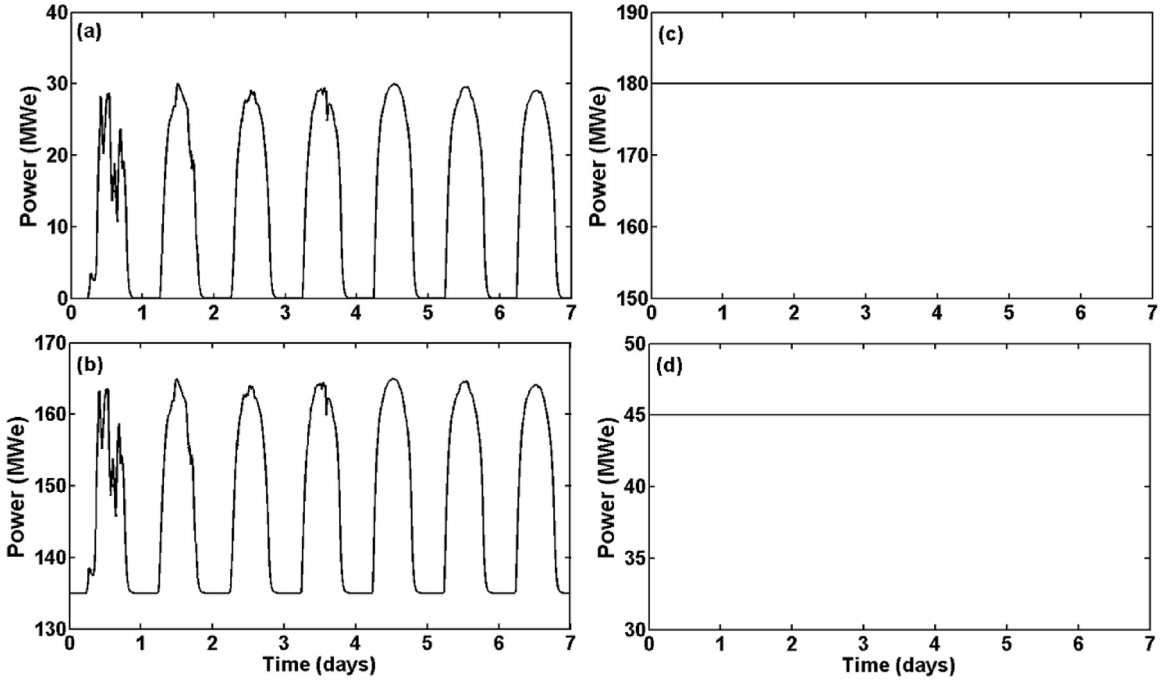

Fig. 11. Load/generation profiles for Case 4: (a) REN (PV solar) power generation, (b) optimal dispatch schedule corresponding to the maximization of the NPV, (c) net load considering the VEL in the RO plant and electricity demand on the grid, and (d) VEL.

reserves (i.e., regulating, ramping, and load following). Based on the findings, RO plants should be considered in the planning and selection process for supporting ancillary services in wholesale energy markets. Their operational flexibility and the variety of potential HES systems configurations in which they can be integrated make them an ideal candidate from a technical point of view.

Acknowledgments

This research is supported by the Energy Security Initiative and the N-R HES (Nuclear-Renewable Hybrid Energy Systems) Program at INL (Idaho National Laboratory) under the U.S. Department of Energy contract DE-AC07-05ID14517. The authors would like to acknowledge the leadership of Drs. Shannon M. Bragg-Sitton and Richard D. Boardman in the (N-R HES) Program at INL, whose contributions made this work possible.

Appendix A. Empirical equations for the saline water properties

Following empirical equations are used to estimate relevant properties of the saline water properties that are required for modeling:

$$D_{NaCl} = 6.725 \times 10^{-6} \exp\left(1.546 \times 10^{-4} C_{b,NaCl} - \frac{2513}{T_b}\right) \tag{A.1}$$

$$\mu_{NaCl} = \mu_{H_2O}\left[1 + A\left(S_b \times 10^6\right) + B\left(S_b \times 10^6\right)^2\right] \tag{A.2}$$

subject to

$$\mu_{H_2O} = 4.2844 \times 10^{-5} + \left[0.157(T_b - 273.15 + 64.993)^2 - 91.296\right]^{-1} \tag{A.3}$$

$$A = 1.541 + 1.998 \times 10^{-2}(T_b - 273.15) - 9.52 \times 10^{-5}(T_b - 273.15)^2 \tag{A.4}$$

$$B = 7.974 - 7.561 \times 10^{-2}(T_b - 273.15) + 4.724 \times 10^{-4}(T_b - 273.15)^2 \tag{A.5}$$

Appendix B. Hydraulic pressure loss along a spiral-wound element

The hydraulic pressure drop along a spiral-wound element can be described by the postulated characteristic:

$$\Delta p_{hydr} = \left(\frac{\lambda \rho_b v_{zb}^2}{2 d_h}\right) \tag{B.1}$$

$$\lambda = 6.23 Re_b^{-0.3} \tag{B.2}$$

$$Re_b = \frac{\rho_b v_{zb} d_h}{\mu_{NaCl}} \tag{B.3}$$

$$v_{zb} = \frac{v_{zf} + v_{zr}}{2} \tag{B.4}$$

Eq. (B.3) may only be valid in the tested flow regime, i.e., $100 < Re_b < 1000$ [31].

Appendix C. Case study data

Table C.1
Model parameters for the FilmTech 8″ BW30-400 membrane [25,34].

Symbol	Description	Unit	Value
l_{BR}	Brine channel length of an RO element	m	0.8665
h_{BR}	Brine channel height of an RO element	m	7.112×10^{-4}
h_{sp}	Spacer thickness	m	7.112×10^{-4}
w_{BR}	Brine channel width of an RO element	m	1.34
n_l	Number of leaves per one RO module	–	16
ϕ_{BR}	Overall void fraction of the brine channel	–	0.9
a_{sp}	Specific surface area of the spacer	m^{-1}	11,249
d_h	Hydraulic diameter	m	9.1×10^{-4}
A_m	Total membrane area per one RO module	m^2 [ft^2]	37.2 [400]
A_s	Membrane area occupied by precipitation	m^2 [ft^2]	1.86[a] [20]
α_1	Constant for solvent transport	–	8.6464
α_2	Constant for solvent transport	bar^{-1}	0.0149
β_1	Constant for solute transport	–	14.648
L_{v0}	Intrinsic solvent transport parameter	m Pa^{-1} s^{-1}	1.042×10^{-11}
L_{s0}	Intrinsic solute transport parameter	m s^{-1}	1.333×10^{-8}

[a] Equivalent membrane fouling in terms of percentage at this value is 5%.

Table C.2
Parameters of the FOPTD model approximations and corresponding PI controller settings based on the DS method.

Symbol	Description	Value	
		VEL controller	Feed pressure controller
K	Model gain	480 (W rpm^{-1})	−13.2 (bar)
τ	Time constant	20 (s)	30.6 (s)
τ_c	Desired closed-loop time constant	6.67[a] (s)	10.2[a] (s)
θ	Time delay	0	0
K_c	Controller gain	0.00625 (rpm W^{-1})	−0.228 (bar^{-1})
τ_I	Integral time	20 (s)	30.6 (s)
y^{min}	Lower bound on controller output	600 (rpm)	0.05
y^{max}	Upper bound on controller output	3000 (rpm)	1

[a] Setting $\tau_c = \tau_I/3$ means that the desired closed-loop response is three times faster than the open-loop response.

Nomenclature

Acronyms

BWRO	brackish water reverse osmosis
CVs	controlled variables
DS	direct synthesis
ESE	energy storage element
FLR	flexible load resource
FOPTD	first-order-plus-time-delay
FPP	freshwater production plant
GHG	greenhouse gas
HES	hybrid energy systems
HP	high-pressure
ISO	independent system operator
MGPD	million gallons per day
MVs	manipulated variables
NPV	net present value
PCV	pressure control valve
PHG	primary heat generation
PHG-TEC	PHG coupled with TEC
PI	proportional-integral
PV	photovoltaic
REN	renewable
RG	required generation
RO	reverse osmosis
SWRO	spiral-wound reverse osmosis
TDS	total dissolved solids
TEC	thermal-to-electrical conversion
VEL	variable electrical load

Parameters and variables

a_{sp}	specific surface area of the spacer (m^{-1})
A_m	total membrane area per one RO module (m^2)
A_s	membrane area occupied by precipitation (m^2)
C	solute mass concentration (kg m^{-3})
C_m	solute mass concentration at the membrane surface (kg m^{-3})
$\overline{C}_m$	average solute mass concentration at the membrane surface (kg m^{-3})
d_h	hydraulic diameter (m)
D_{NaCl}	solute diffusion coefficient of the H_2O–NaCl solution (m^2 s^{-1})
$\hat{h}$	fluid specific enthalpy (J kg^{-1})
h_{sp}	spacer thickness (m)
h_{BR}	brine channel height of an RO element (m)
$\overline{J}_s$	average solute flux (kg m^{-2} s^{-1})
$\overline{J}_v$	average solvent flux (m s^{-1})
J_{vz}	local solvent flux (m s^{-1})
k_{NaCl}	mass transfer coefficient of NaCl (m s^{-1})
K	model gain ("W rpm^{-1}" for the VEL controller or "bar" for the feed pressure controller)
K_c	controller gain ("rpm W^{-1}" for the VEL controller or "bar^{-1}" for the feed pressure controller)
l_m	membrane length (m)
l_{BR}	brine channel length of an RO element (m)
L_{s0}	intrinsic solute transport parameter (m s^{-1})
L_{v0}	intrinsic solvent transport parameter (m Pa^{-1} s^{-1})

$L_{E,\,sp}$	VEL set point (MW_e)
MW	molecular weight (kg mol^{-1})
n_l	number of leaves (or flat sheets) per one RO module
N_{pump}	number of HP feed pumps
N_M	number of SWRO modules per one pressure vessel (or stage)
N_{ST}	number of stages
N_{TR}	number of RO unit trains
N_{VE}	number of pressure vessels per one RO unit train
p	pressure (Pa)
$P_{f,\,sp}$	feed pressure set point (bar)
$P_{I,\,RO}$	power consumption in RO process (MW_e)
$P_{I,\,RO,\,n}$	rated electrical load in the FPP (MW_e)
Q	volumetric flow rate ($m^3\ s^{-1}$)
R	ideal gas constant (J mol^{-1} K^{-1})
Re	Reynolds number
R_s	salt rejection (%)
R_w	overall water recovery (%)
R_{w1}	water recovery in the first stage (%)
R_{w2}	water recovery in the second stage (%)
S	salinity (ppm)
$\overline{S}$	average salinity (ppm)
Δt	simulation output interval (s)
T	temperature (K)
$\hat{u}$	specific internal energy (J kg^{-1})
v_z	brine velocity along the z-axis (axial) in the brine channel of an RO element (m s^{-1})
V_{op}	valve opening (%)
V_{BR}	brine channel volume of an RO element excluding the volume occupied by the spacer (m^3)
w_m	membrane width (m)
w_{BR}	brine channel width of an RO element (m)
y	bound on controller output ("rpm" for the VEL controller or dimensionless for the feed pressure controller)
α_1	membrane-specific parameter for solvent transport
α_2	membrane-specific parameter for solvent transport (bar^{-1})
β_1	membrane-specific parameter for solute transport
ϵ_{pump}	pump efficiency (%)
θ	time delay (s)
λ	friction factor
μ_{H20}	dynamic viscosity of pure water (Pa s)
μ_{NaCl}	dynamic viscosity of the H_2O–NaCl solution (Pa s)
π	osmotic pressure (Pa)
ρ	density of solution (kg m^{-3})
τ	time constant (s)
τ_c	desired closed-loop time constant (s)
τ_I	integral time (s)
ϕ_{BR}	overall void fraction of the brine channel
ω	pump shaft rotational speed (rpm)

Subscripts

b	bulk (average between feed and retentate) stream
f	feed (saline water) stream
i	dissolved solid (component) in an aqueous solution
$NaCl$	sodium chloride molecule
p	permeate (fresh water) stream
r	retentate (concentrate) stream
t	time

Superscripts

$exit$	at the RO module exit
max	maximum limit
min	minimum limit

References

[1] Wuebbles DJ, Jain AK. Concerns about climate change and the role of fossil fuel use. Fuel Process Technol 2001;71(1–3):99–119.

[2] Sims REH, Rogner H-H, Gregory K. Carbon emission and mitigation cost comparisons between fossil fuel, nuclear and renewable energy resources for electricity generation. Energy Policy 2003;31(13):1315–26.

[3] Ruth MF, Zinaman OR, Antkowiak M, Boardman RD, Cherry RS, Bazilian MD. Nuclear-renewable hybrid energy systems: opportunities, interconnections, and needs. Energy Convers Manag 2014;78:684–94.

[4] Bragg-Sitton SM, Boardman R, Rabiti C, Kim JS, McKellar M, Sabharwall P, et al. Nuclear-renewable hybrid energy systems: 2016 technology development program plan. Idaho Falls (ID): Idaho National Laboratory, Nuclear Science and Technology Division; 2016 Mar. Report No.: INL/EXT-16–38165. Contract No.: DE-AC07-05ID14517. Sponsored by the U.S. Department of Energy.

[5] Bragg-Sitton SM, Boardman RD. Overview of U.S. DOE research and development of nuclear-renewable hybrid energy systems. Trans Am Nucl Soc 2015;112:113–6.

[6] Hamsic N, Schmelter A, Mohd A, Ortjohann E, Schultze E, Tuckey A, et al. Increasing renewable energy penetration in isolated grids using a flywheel energy storage system. In: Proceedings of the International Conference on Power Engineering, Energy and Electrical Drives; 2007 Apr 12-14. p. 195–200. Setúbal, Portugal.

[7] Hittinger E, Whitacre JF, Apt J. Compensating for wind variability using co-located natural gas generation and energy storage. Energy Syst 2010;1(4):417–39.

[8] Weisser D, Garcia RS. Instantaneous wind energy penetration in isolated electricity grids: concepts and review. Renew Energy 2005;30(8):1299–308.

[9] Cherry RS, Aumeier SE, Boardman RD. Large hybrid energy systems for making low CO_2 load-following power and synthetic fuel. Energy & Environ Sci 2012;5(2):5489–97.

[10] Panwar M, Mohanpurkar M, Osorio JD, Hovsapian R. Significance of dynamic and transient analysis in the design and operation of hybrid energy systems. In: Proceedings of the 9th international Topical meeting on nuclear plant instrumentation, control, and human machine interface technologies [internet]; 2015 Feb 23-26. Charlotte, NC. Available: http://www.osti.gov/scitech//servlets/purl/1179379/.

[11] Garcia HE, Chen J, Kim JS, McKellar MG, Deason WR, Vilim RB, et al. Nuclear hybrid energy systems - regional studies: west Texas & Northeastern Arizona. Idaho Falls (ID): Idaho National Laboratory, Nuclear Science and Technology Division; 2015 Apr. Report No.: INL/EXT-15–34503. Contract No.: DE-AC07-05ID14517. Sponsored by the U.S. Department of Energy.

[12] Eichman J, Harrison KW, Peters M. Novel electrolyzer applications: providing more than just hydrogen. Boulder (CO): National Renewable Energy Laboratory; 2014 Sep. Report No.: NREL/TP-5400–61758. Contract No.: DE-AC36-08GO28308. Sponsored by the U.S. Department of Energy.

[13] Bragg-Sitton SM, Boardman RD, Cherry RS, Deason WR, McKellar MG. An analysis of methanol and hydrogen production via high-temperature electrolysis using the sodium cooled advanced fast reactor. Idaho Falls (ID): Idaho National Laboratory, Nuclear Science and Technology Division; 2014 Mar. Report No.: INL/EXT-14–31642. Contract No.: DE-AC07-05ID14517. Sponsored by the U.S. Department of Energy.

[14] Cherry RS, Breckenridge RP, Boardman RD, Bell D, Foulke T, Lichtenberger J. Preliminary feasibility of value-added products from cogeneration and hybrid energy systems in Wyoming. Idaho Falls (ID): Idaho National Laboratory, Energy and Environmental Science and Technology Division; 2012 Nov. Report No.: INL/EXT-12–27249. Contract No.: DE-AC07-05ID14517. Sponsored by the U.S. Department of Energy.

[15] Wood R, Boardman R, Patterson M. Nuclear-integrated methanol-to gasoline production analysis. Idaho Falls (ID): Idaho National Laboratory, Energy and Environmental Science and Technology Division; 2010 May. Report No.: TEV-667. Contract No.: DE-AC07–05ID14517. Sponsored by the U.S. Department of Energy.

[16] Garcia HE, Mohanty A, Lin W-C, Cherry RS. Dynamic analysis of hybrid energy systems under flexible operation and variable renewable generation – Part I: dynamic performance analysis. Energy 2013;52:1–16.

[17] Kalogirou SA. Seawater desalination using renewable energy sources. Prog Energy Combust Sci 2005;31(3):242–81.

[18] Kim JS, Garcia HE. Nuclear-renewable hybrid energy system for reverse osmosis desalination process. Trans Am Nucl Soc 2015;112:121–4.

[19] Ghaffour N, Bundschuh J, Mahmoudi H, Goosen MFA. Renewable energy-driven desalination technologies: a comprehensive review on challenges and potential applications of integrated systems. Desalination 2015;356:94–114.

[20] Cherif H, Belhadj J. Large-scale time evaluation for energy estimation of stand-alone hybrid photovoltaic–wind system feeding a reverse osmosis desalination unit. Energy 2011;36(10):6058–67.

[21] Manolakos D, Papadakis G, Papantonis D, Kyritsis S. A simulation-optimisation programme for designing hybrid energy systems for supplying electricity and fresh water through desalination to remote areas: case study: the Merssini village, Donoussa island, Aegean Sea, Greece. Energy 2001;26(7):679–704.

[22] Schwinge J, Neal PR, Wiley DE, Fletcher DF, Fane AG. Spiral wound modules and spacers: review and analysis. J Membr Sci 2004;242(1–2):129–53.

[23] Marriott J, Sørensen E. A general approach to modelling membrane modules.

Chem Eng Sci 2003;58(22):4975–90.
[24] Van Gauwbergen D, Baeyens J. Macroscopic fluid flow conditions in spiral-wound membrane elements. Desalination 1997;110(3):287–99.
[25] Oh H-J, Hwang T-M, Lee S. A simplified simulation model of RO systems for seawater desalination. Desalination 2009;238(1–3):128–39.
[26] Kim YM, Kim SJ, Kim YS, Lee S, Kim IS, Kim JH. Overview of systems engineering approaches for a large-scale seawater desalination plant with a reverse osmosis network. Desalination 2009;238(1–3):312–32.
[27] Driesner T. The system H_2O–NaCl. Part II: correlations for molar volume, enthalpy, and isobaric heat capacity from 0 to 1000°C, 1 to 5000 bar, and 0 to 1 X_{NaCl}. Geochimica Cosmochimica Acta 2007;71(20):4902–19.
[28] Sharqawy MH, Lienhard JH, Zubair SM. Thermophysical properties of seawater: a review of existing correlations and data. Desalination Water Treat 2010;16(1–3):354–80.
[29] Djebedjian B, Gad H, Khaled I, Rayan MA. Optimization of reverse osmosis desalination system using genetic algorithms technique. In: Proceedings of the Twelfth International Water Technology Conference; 2008 Mar 27-30. p. 1047–67. Alexandria, Egypt.
[30] Wijmans JG, Baker RW. The solution-diffusion model: a review. J Membr Sci 1995;107(1–2):1–21.
[31] Schock G, Miquel A. Mass transfer and pressure loss in spiral wound modules. Desalination 1987;64:339–52.
[32] Hyung H, Kim J-H. A mechanistic study on boron rejection by sea water reverse osmosis membranes. J Membr Sci 2006;286(1–2):269–78.
[33] Seader J, Henley E. Separation process principles. second ed. New Jersey: Wiley; 2006.
[34] Avlonitis SA, Pappas M, Moutesidis K. A unified model for the detailed investigation of membrane modules and RO plants performance. Desalination 2007;203(1–3):218–28.
[35] Lee S, Lueptow RM. Membrane rejection of nitrogen compounds. Environ Sci Technol 2001;35(14):3008–18.
[36] Cussler EL. Diffusion: mass transfer in fluid systems. third ed. Cambridge: Cambridge University Press; 2009.
[37] Wilf M, Bartels C. Optimization of seawater RO systems design. Desalination 2005;173(1):1–12.
[38] Zeman LJ, Zydney AL. Microfiltration and ultrafiltration: principles and applications. New York: Marcel Dekker; 1996.
[39] Cheryan M. Ultrafiltration and microfiltration handbook. second ed. Florida: CRC Press; 1998.
[40] Bartels C, Franks R, Rybar S, Schierach M, Wilf M. The effect of feed ionic strength on salt passage through reverse osmosis membranes. Desalination 2005;184(1–3):185–95.
[41] Zhu A, Christofides PD, Cohen Y. Minimization of energy consumption for a two-pass membrane desalination: effect of energy recovery, membrane rejection and retentate recycling. J Membr Sci 2009;339(1–2):126–37.
[42] Zhu A, Christofides PD, Cohen Y. Energy consumption optimization of reverse osmosis membrane water desalination subject to feed salinity fluctuation. Industrial Eng Chem Res 2009;48(21):9581–9.
[43] Greenlee LF, Lawler DF, Freeman BD, Marrot B, Moulin P. Reverse osmosis desalination: water sources, technology, and today's challenges. Water Res 2009;43(9):2317–48.
[44] Seborg DE, Mellichamp DA, Edgar TF, Doyle III FJ. Process dynamics and control. third ed. New Jersey: Wiley; 2010.
[45] Landau CR. Optimal Tilt of Solar Panels [Internet]. [updated 2014 Apr 16; cited 2015 Mar 23]. Available: http://www.solarpaneltilt.com/.
[46] Garcia HE, Chen J, Kim JS, Vilim RB, Binder WR, Bragg-Sitton SM, et al. Dynamic performance analysis of two regional nuclear hybrid energy systems. Energy 2016;107:234–58.
[47] Honsberg C, Bowden S. Solar Radiation on a Tilted Surface [Internet]. [updated 2014 Feb 5; cited 2015 Mar 23]. Available: http://www.pveducation.org/pvcdrom/properties-of-sunlight/solar-radiation-on-tilted-surface.
[48] Honsberg C, Bowden S. Making Use of TMY Data [Internet]. [updated 2014 Feb 5; cited 2015 Mar 23]. Available: http://www.pveducation.org/pvcdrom/properties-of-sunlight/making-use-of-TMY.
[49] Dobos AP. PVWatts version 5 manual. Boulder (CO): National Renewable Energy Laboratory; 2014 Sep. Report No.: NREL/TP-6A20–62641. Contract No.: DE-AC36-08GO28308. Sponsored by the U.S. Department of Energy.
[50] Skoplaki E, Palyvos J. On the temperature dependence of photovoltaic module electrical performance: a review of efficiency/power correlations. Sol energy 2009;83(5):614–24.
[51] Jie J, Hua Y, Wei H, Gang P, Jianping L, Bin J. Modeling of a novel Trombe wall with PV cells. Build Environ 2007;42(3):1544–52.
[52] Fritzson P. Principles of object-oriented modeling and simulation with modelica 3.3: a cyber-physical approach. second ed. New Jersey: Wiley; 2014.
[53] Afshar MH, Rohani M. Water hammer simulation by implicit method of characteristic. Int J Press Vessels Pip 2008;85(12):851–9.
[54] Chen J, Garcia HE, Kim JS, Bragg-Sitton SM. Operation optimization of nuclear hybrid energy systems. Nucl Technol 2016 [in press].